

1 **Single molecule imaging of the central dogma reveals myosin-2A gene
2 expression is regulated by contextual translational buffering**

3 O'Neil Wiggan^{1*} and Timothy J. Stasevich^{1,2*}

4 ¹Department of Biochemistry and Molecular Biology, Colorado State University, Fort
5 Collins, CO, 80525

6 ¹Department of Biochemistry and Molecular Biology, Colorado State University, Fort
7 Collins, CO, 80525

8 ²Cell Biology Center and World Research Hub Initiative, Tokyo Institute of Technology,
9 Yokohama, Japan.

10 *Corresponding authors: oneil.wiggan@colostate.edu, tim.stasevich@colostate.edu

11

12 **Abstract**

13 While protein homeostasis is a hallmark of gene regulation, unraveling the hidden
14 regulatory mechanisms that maintain homeostasis is difficult using traditional methods.
15 To confront this problem, we CRISPR engineered a human cell line with multiple tags in
16 the endogenous MYH9 gene, which encodes the essential and ubiquitous myosin-2A
17 cytoskeletal motor. Using these cells, we imaged MYH9 transcription, translation, and
18 mature mRNA and protein in distinct colors, enabling a full dissection of the central
19 dogma. Our data show that MYH9 transcription is upregulated in an SRF-dependent
20 manner in response to cytoskeletal cues and that MYH9 translation can either buffer or
21 match the transcriptional response depending on context. Upon knockdown of actin-
22 depolymerizing proteins like cofilin, translation efficiency drops by a factor of two to buffer
23 strong transcriptional upregulation, likely to help prevent excessive myosin activity. In
24 contrast, following serum stimulation, translation matches the transcriptional response to
25 readily establish equilibrium. Our results identify contextual translational buffering as an
26 important regulatory mechanism driving stable MYH9 expression. They also demonstrate
27 the power and broad applicability of our cell line, which can now be used to accurately
28 quantify central dogma dynamics in response to diverse forms of cellular perturbations.

29

30

31

32 Introduction

33 A grand challenge in cell biology is to image the full central dogma as it plays out in living
34 cells, one molecule at a time. Although tags now exist to separately image individual
35 proteins, mRNA, and sites of transcription and translation¹⁻⁴, the tags are rarely combined
36 into a single experimental system and even more rarely incorporated into endogenous
37 genes⁵. This has made it difficult to pinpoint at what level gene regulation occurs⁶; for
38 example, does a decrease in total protein reflect less translation or more degradation?
39 Alternatively, if levels remain unchanged, does that mean that transcription and
40 translation are also unchanged, or could they instead be changing together, but in
41 opposition?

42 The MYH9 gene exemplifies this challenge. MYH9 encodes non-muscle myosin-2A heavy
43 chain, a motor protein that assembles into bipolar filaments that use ATP to power
44 contraction of the actomyosin cytoskeleton⁷. This contraction generates intracellular
45 forces that govern cell architecture, migration, adhesion, and division. MYH9 is essential
46 and, like beta-actin, is sometimes categorized as a housekeeping gene, implying stable
47 expression and minimal regulation^{7, 8}. Consistent with this, myosin activity is thought to
48 be mainly regulated by post-translational phosphorylation, a dynamic and reversible mark
49 that activates myosin motors⁹. On the other hand, the MYH9 gene has also been
50 categorized as both an oncogene and tumor suppressor^{10, 11}, and some studies have
51 even shown cancer metastasis relies on MYH9 upregulation¹². These studies highlight
52 the need to better understand MYH9 regulation and they suggest both too little and too
53 much MYH9 expression is detrimental. This raises an important and generalizable
54 question: do multiple competing regulatory mechanisms strictly enforce the stable
55 expression of genes like MYH9, or does the stability instead arise from a lack of
56 regulation?

57 To directly address this question and better understand how gene expression
58 homeostasis can be established and maintained, we engineered a unique human cell line
59 with multiple tags knocked into the endogenous MYH9 gene. By co-tracking MYH9
60 transcription, translation, and total mRNA at the level of single molecules, we show that
61 translational regulation is a critical aspect of MYH9 expression, one that can be
62 independently regulated from transcription. During cell division or upon the loss of actin
63 depolymerizing proteins, translation buffers transcriptional upregulation, presumably to
64 offset detrimental myosin-2A overexpression. In contrast, upon a release from serum
65 starvation, translation increases in sync with transcription to quickly establish cellular
66 phenotypic changes. Collectively, our results highlight the complexity of the central dogma
67 and provide compelling evidence that even apparently stable genes like MYH9 can hide
68 multilayered and context-dependent gene regulatory mechanisms.

69

70

71 Results

72 A system to co-image endogenous transcription and translation with single- 73 molecule precision

74 To evaluate gene expression for endogenous MYH9 in human HeLa cells, we performed
75 sequential rounds of CRISPR Cas9 gene editing. First, we incorporated an in-frame C-
76 terminal mClover tag (a GFP variant referred to herein as GFP) at the end of exon 40
77 followed by 24×MS2 stem loops upstream of the native 3' untranslated region. Next, we

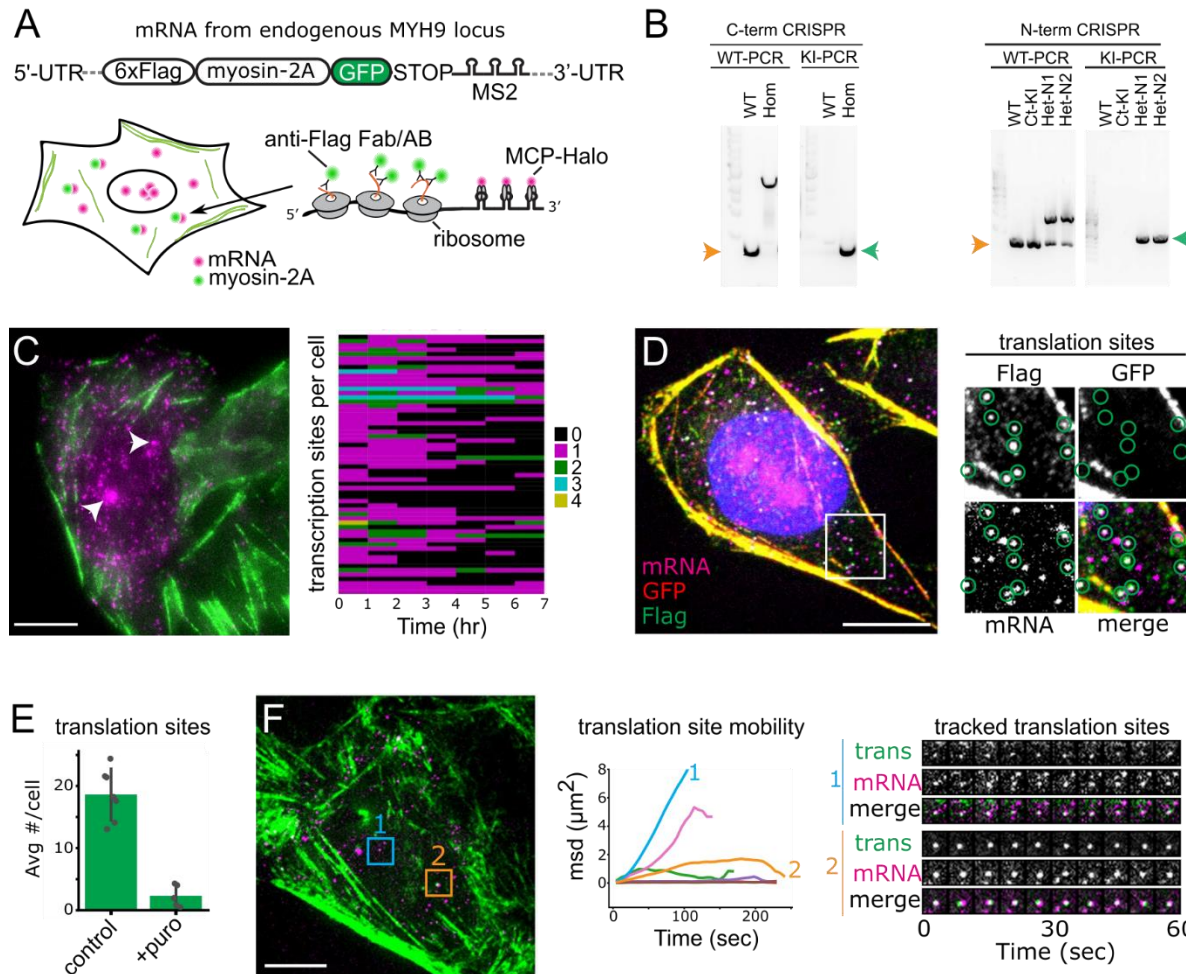


Fig. 1 A cell line for dissecting the central dogma with single-molecule precision. **A.** Top, schematic of a tagged MYH9 transcript in CRISPR modified eMyo2AGFP cells. Below, cartoon of an eMyo2AGFP cell expressing myo2A-encoding mRNA (magenta) myo2A protein (green) and translation sites (colocalized foci of mRNA and protein). **B.** Genomic PCR for detection of wild type (orange arrow) or knock-in (green arrow, homo or heterozygous) alleles following successive rounds of CRISPR editing. **C.** Live cell image of eMyo2AGFP cell with myo2A-GFP protein (green) and mRNA (magenta), arrowheads show mRNA transcription foci. Heatmap of numbers of transcription sites over 1hr intervals, each row corresponds to one cell (right). **D.** Representative confocal fixed cell image showing myo2A mRNAs without translation signals (magenta), and translating mRNAs marked by colocalized mRNA and Flag-my2A (green) but absence of mature myo2A-GFP (red). Boxed region is enlarged (right) with translation sites encircled. **E.** Quantification of loss of translation sites following puromycin treatment. Mean \pm SD, 580 cells control and 285 cells puro. **F.** Live cell confocal image of anti-FLAG Fab labeled Flag-my2A (green) and mRNA (magenta). Mean squared displacement (msd) plots for 7 mRNA tracks (center), including translation site mobility of a single mRNA (1) or an mRNA cluster (2) for boxed regions also shown in time series images, right. Scale bars 10 μ m.

78 integrated an N-terminal 6×Flag tagged mCherry after the start codon (**Figs. 1A, S1A**).
79 Following successive rounds of gene editing, we isolated subclones where both MYH9
80 alleles were C-terminally tagged and one was N-terminally tagged (**Fig. 1B**). The tags did
81 not appear to impair MYH9 function because Myo2A-GFP localized to actomyosin
82 structures, including cortical bundles and stress fibers (**Fig. 1C**) and MYH9 mRNA levels
83 were not significantly different than unedited cells (**Fig. S1B**). Using these cells we could
84 visualize mature Myo2A proteins in green (GFP), nascent Myo2A peptide chains at
85 translation sites in red (using Cy3-conjugated anti-Flag antibodies), and Myo2A-endoding
86 mRNA in far-red (using Halo-tagged MS2 coat protein with JF646 ligand), enabling a full
87 dissection of the central dogma in separate colors. Hereafter we refer to this cell line as
88 eMyo2AGFP.

89 To demonstrate our ability to detect both transcription and translation with single molecule
90 sensitivity in eMyo2AGFP cells, we first focused on steady-state MYH9 expression. Live
91 imaging revealed bursts of transcription at between one and four sites per cell (**Fig. 1C**
92 and **Movie S1**), as would be expected for a diploid locus. Cells had tens to hundreds of
93 MYH9 transcripts in the nucleus and cytoplasm (**Fig. 1C**). To identify which were
94 translated, we immunostained fixed cells and looked for bright FLAG signals that
95 overlapped with mRNA yet lacked GFP (since GFP takes time to mature after translation).
96 According to this metric, many cytoplasmic mRNA were translation sites (**Fig. 1D**) and
97 these reassuringly disappeared upon treatment with the translational inhibitor puromycin
98 (**Fig. 1E**).

99 To further characterize individual Myo2A translation sites, we performed live imaging with
100 anti-FLAG intrabodies ⁴. This revealed diverse behaviors, from fast unidirectional
101 movement to slow, nearly immobile diffusion (**Fig. 1F and Movie S2**). We usually
102 detected translation from single mRNAs, although a small fraction (<1%) were in bright
103 clusters, reminiscent of translation factories (**Fig. 1F, spot 2**) (ref 13). Altogether, our data
104 demonstrate eMyo2A cells are versatile tools to comprehensively examine broad aspects
105 of MYH9 gene expression with single molecule precision.

106

107 **MYH9 translation efficiency is high and undergoes regulation during cell division**

108 Confident in our ability to detect individual mRNA and translation sites, we next set out to
109 quantify their average numbers in cells. We used fixed cells for this analysis because we
110 obtained better signal to noise and tag saturation than is possible in live cells. On average,
111 eMyo2AGFP cells contained 90 ± 47 total mRNA per cell (**Fig. 2A**). Of these, 53 ± 29
112 were in the cytoplasm, 20 ± 10 of which were being translated (we did not detect nuclear
113 translation). Separately, the fraction of cytoplasmic mRNAs translating the FLAG tag was
114 measured at $46 \pm 6\%$ (**Fig. 2B**). Since we only expect half of the cytoplasmic transcripts
115 to encode the FLAG tag in the first place (due to its heterozygous insertion), we estimate
116 the translation efficiency to be double our measured cytoplasmic fraction $\sim 93\%$ (**Fig. 2B**,

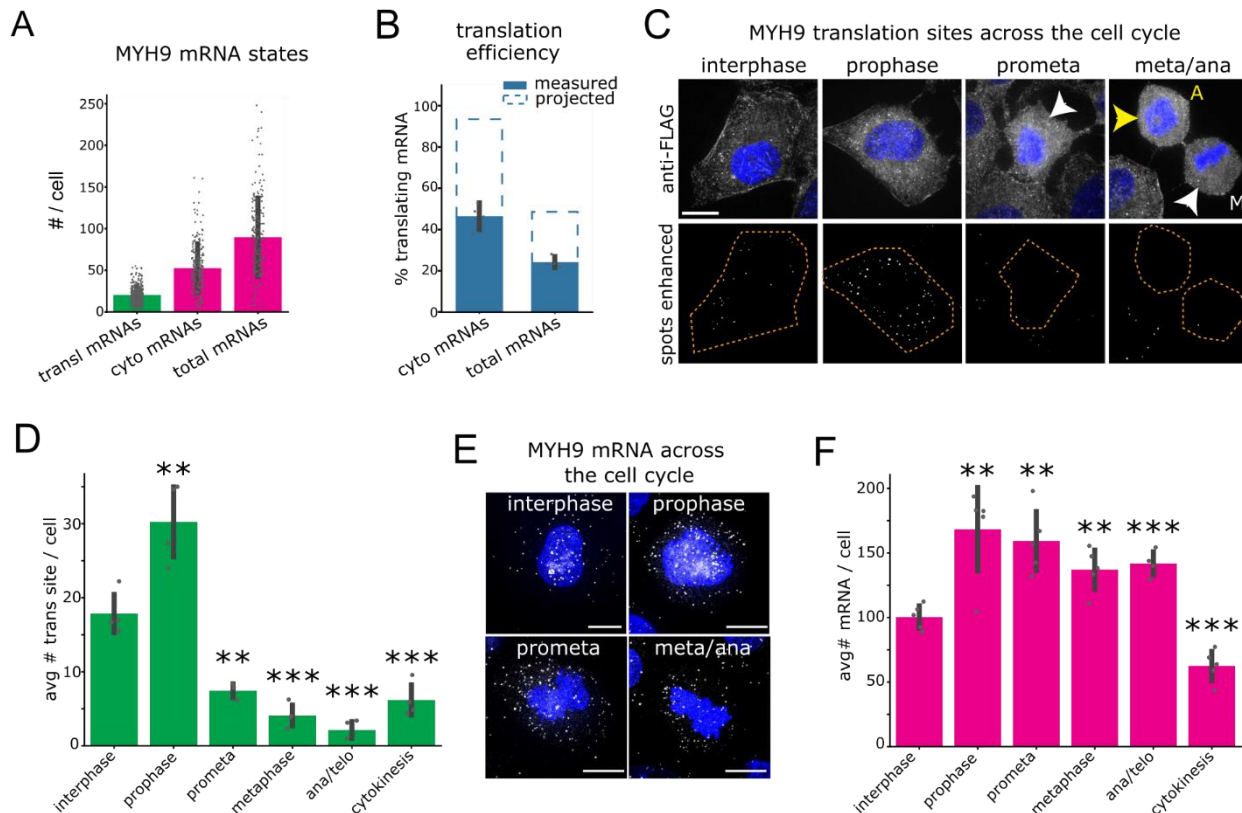


Fig. 2 MYH9 translation is downregulated during cell division. **A.** Quantification of mRNAs and translation. Mean \pm SD. **B.** Quantification of translating mRNA percentage. Note, in eMyo2AGFP cells there are two labeled MYH9 mRNA alleles, of which only one detects translation (measured) Mean \pm SD, n= 361 cells. Dashed line (projected) shows projected % translation accounting for two alleles. **C.** Representative confocal immunofluorescence images of MYH9 translation sites labeled by anti-Flag and for DNA (blue). A-anaphase cell, M-metaphase cell. Lower panels show spot fluorescence enhanced by a LOG filter for outlined cells. **D.** Quantification of translation sites across the cell cycle. Mean \pm SD, interphase n= 312 cells, mitotic n \geq 20 cells/phase. **E.** Fluorescence images of MYH9 mRNAs labeled by Halo-MCP were imaged in fixed cells at different stages of the cell cycle (DNA in blue). **F.** Quantification of the average number of mRNA per cell. Mean \pm SD, interphase n= 122 cells, mitotic n \geq 18 cells/phase. Scale bars 10 μ m. * ***p \leq 0.01, ***p \leq 0.001, Welch's t-test.

117 **projected).** These data therefore suggest that the majority of cytoplasmic MYH9
 118 transcripts were being translated.

119 The high efficiency of MYH9 translation is perhaps not surprising given the abundance of
 120 myosin-2A required to form the actomyosin cytoskeleton. However, this left us wondering
 121 if MYH9 translation is subject to regulation. To test this, we imaged eMyo2AGFP cells
 122 across the cell cycle (**Fig. 2C**), avoiding the use of drugs commonly used to synchronize
 123 cells (which can suffer from artifacts ¹⁴). We hypothesized translation might be modulated
 124 during cell division since myosin-2 motors are known to play an important and highly
 125 conserved role in contractile ring assembly. Our analysis confirmed this: we observed a
 126 sharp increase in the number of translation sites at prophase relative to interphase,
 127 followed by a dramatic drop from prometaphase through cytokinesis (**Fig. 2D**).
 128 Interestingly, while the initial increase could be explained by a commensurate increase in
 129 MYH9 mRNA levels, the later drop did not follow the mRNA pattern (**Fig. 2E, F**). Thus, it

130 appears that MYH9 translation is downregulated independently from transcription just
131 after prophase.

132 Rounded mitotic cells generally have reduced cell surface area relative to those of
133 interphase (**Fig. S2A**) and there was a strong positive correlation between cell size and
134 MYH9 translation (**Fig. S2B**), so we explored whether cell size alterations could account
135 for the reduced translation. However, normalization of MYH9 translation sites to cell area
136 still showed reduced MYH9 translation for cells in prometaphase onwards (**Fig. S2C**). We
137 conclude that reduced mitotic MYH9 translation is not a function of decreased cell areas.
138 In summary, our results identify existence of a post-transcriptional mechanism that
139 modulates the overall high efficiency of MYH9 mRNA translation in a cell-cycle dependent
140 manner.

141

142 ***Silencing of actin depolymerizing proteins stimulates SRF-dependent MYH9*** 143 ***transcriptional bursts***

144 Having characterized MYH9 expression in steady state, we now turned our attention to
145 MYH9 stimulation. In an earlier study we showed that knockdown of two closely related
146 actin depolymerizing proteins, cofilin and ADF, results in detrimental myosin contractile
147 activity¹⁵. Over a period of 72 hours, this leads to excessive forces in cells that contort
148 nuclei into tortured shapes that are reminiscent of those founds in tumors (**Fig. 3A**). This
149 detrimental phenotype can be rescued by co-inhibiting myosin during cofilin/ADF

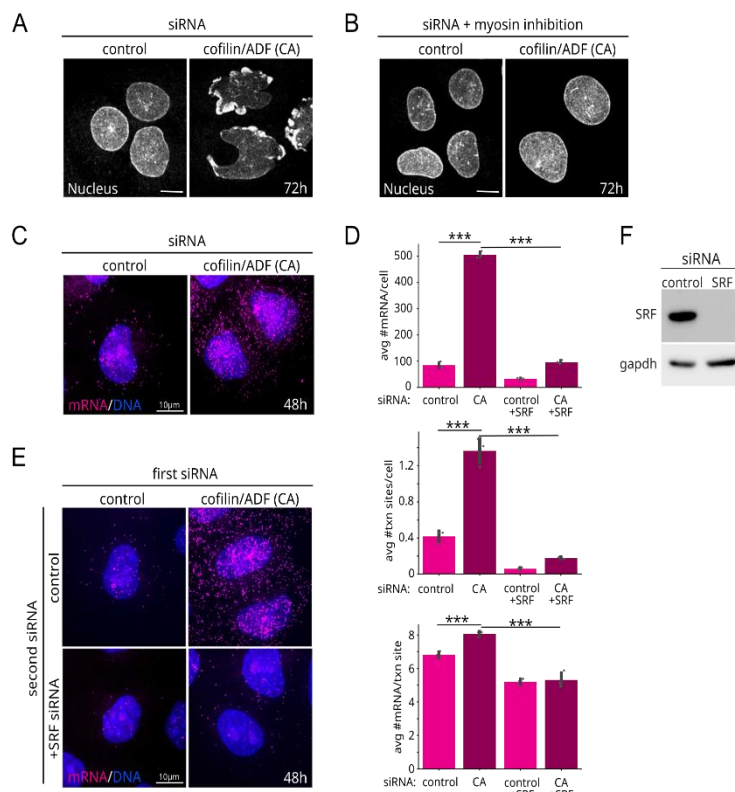


Fig. 3 SRF-dependent MYH9 transcriptional bursts in response to knock-down of actin polymerizing proteins. A,B. Representative immunofluorescence images of nuclear envelope labeled cells depicting nuclear dysmorphology induced by cofilin/ADF silencing (A) and rescue by myosin inhibition via Y27632 treatment (B). **C-E.** MCP-Halo fluorescence images of MYH9 mRNA (magenta, C and E) and quantification of MYH9 mRNAs (D, top), transcription sites (D, middle) and burst amplitude (D, bottom) following cofilin/ADF silencing (C) and co-silencing of SRF (E). Scale bars 10 µm. Values are mean ± SD, n ≥ 186 cells/treatment. *** p ≤ 0.001, Welch's t-test. **F.** Immunoblot of SRF siRNA silencing.

150 silencing, demonstrating the phenotype is due to excessive myosin-based forces (**Fig. 3B, and ref 16** for quantification). We previously showed this is in part due to enhanced
151 association of myosin with F-actin (since cofilin competes with myosin for F-actin).
152 However, *in vivo* studies of ADF null mice suggested a link between defective actin
153 dynamics and actomyosin gene expression ¹⁷. This led us to ask if deregulated MYH9
154 expression was also partly responsible.
155

156 To test this, we silenced cofilin/ADF expression using siRNA in eMyo2AGFP cells (**Fig. 3C**). Consistent with MYH9 deregulation, the number of MYH9 mRNA per cell
157 dramatically increased from ~100 to ~500 after 48 hours (**Fig. 3D, top, Control & CA**;
158 note at 72 h, when nuclei are contorted, there were too many mRNA to count). The mRNA
159 increase was caused by a roughly 3-fold increase in the number of transcription sites per
160 cell (burst frequency; **Fig. 3D, middle, Control & CA**) in combination with a modest
161 increase of ~1.3 mRNA per transcription site (burst amplitude; **Fig. 3D, bottom, Control**
162 **vs CA**). Live-cell analysis confirmed increased temporal MYH9 burst activity for
163 cofilin/ADF silenced cells (**Fig. S3C**). To see if there were additional changes to
164 transcription kinetics after an allele is activated, we tracked active sites over a period of
165 2-5 hours (**Fig. S3A and Movie S3**). However, classification of their fluctuations using a
166 three-state Hidden Markov Model ^{18, 19} revealed no significant changes (**Fig. S3B**).
167 Together, these data suggest the major impact of cofilin/ADF knockdown on MYH9
168 transcription is enhanced activation.
169

170 Stimulation of transcription via simultaneous frequency and amplitude modulation is not
171 universal ²⁰, but has been observed for genes such as beta-actin ²¹, whose transcription
172 is linked to a master cytoskeleton transcription factor, Serum Response Factor (SRF) ²².
173 As MYH9 is also a putative target of SRF, we wondered if SRF is responsible for the
174 enhanced transcription. To see if this was the case, we repeated our cofilin/ADF
175 knockdown experiments, but in addition we co-silenced SRF (**Fig. 3E, F**). Remarkably,
176 this almost completely blocked the increase in MYH9 mRNA levels, attenuating both burst
177 frequency and amplitude (**Fig. 3D, Control+SRF & CA+SRF**). These results identify SRF
178 as an essential mediator of transcription burst dynamics for the MYH9 gene in both basal
179 and stimulated conditions. The data also argue that elevated MYH9 mRNA levels
180 following cofilin/ADF loss results from increased transcription and not to other
181 possibilities, such as mRNA stabilization.

182 ***MYH9 transcription is linked to cytoskeletal signaling that promote MKL1 nuclear*** 183 ***localization***

184 By what mechanism does loss of cofilin/ADF lead to SRF-dependent MYH9 transcription?
185 This is an important question because cofilin inactivation, just like myosin-2A
186 overexpression, has been linked to cancer ²³. Transcription of cytoskeletal genes by SRF
187 relies on MKL-family cofactors (a.k.a. MAL, MRTF, ref 22). According to a model (**Fig.**
188 **4A**), when G-actin subunits assemble into actin filaments (F-actin), MKL can enter the
189 nucleus with SRF and activate cytoskeletal genes. However, if G-actin levels become
190 sufficiently high, they bind MKL and prevent its translocation into the nucleus, causing

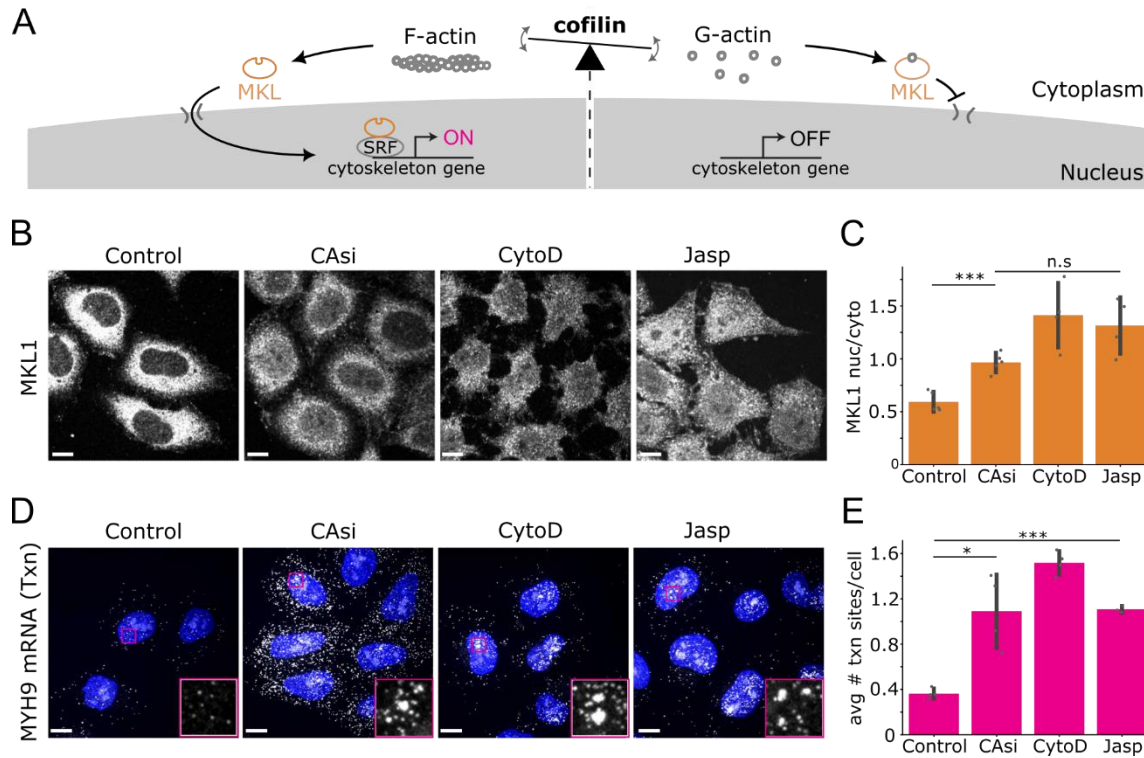


Fig. 4 Altered cytoskeletal dynamics promote MKL1 nuclear localization and MYH9 transcriptional bursts. A. Illustration of model by which cofilin activity and actin dynamics may regulate MKL localization and SRF-dependent cytoskeletal gene expression. **B and C.** Nuclear level confocal immunofluorescence images (B) and quantification (C) of MKL1 nuclear/cytoplasmic distribution for cells treated with cofilin/ADF siRNAs (CASi), cytochalasin D (cytoD) and Jasplakinolide (Jasp). **D and E.** Confocal fluorescence images (D) and quantification (E) of MCP-Halo labeled MYH9 mRNAs. DNA in blue. Insets (D) show enlargement of boxed regions depicting transcription sites. Note, treatment periods are 48h for siRNAs and 2h for drugs. Scale bars 10 μ m. Values are mean \pm SD, n \geq 350 cells/treatment (C), n \geq 330 cells/treatment (E). *p < 0.05, ***p \leq 0.001, n.s not significant by Welch's t-test.

191 attenuation of cytoskeletal gene expression. This cascade ostensibly creates a self-
 192 regulatory feedback loop, dictated by the balance of G- to F-actin.

193 With this model in mind, since cofilin and ADF both disassemble actin filaments into G-
 194 actin, their loss should lower G-actin levels, causing MKL to translocate into the nucleus
 195 and activate cytoskeletal genes like MYH9. To test this model, we measured MKL1 levels
 196 in eMyo2AGFP cells at 48 hours post cofilin/ADF silencing and indeed found a significant
 197 increase in the nuclear fraction of MKL1 (**Fig. 4B, C**). However, the increase was not
 198 particularly striking, as the majority of MKL1 remained in the cytoplasm. We saw a similar
 199 result in a set of related experiments in which we promoted levels of MKL unbound by G-
 200 actin using drugs (cytochalasin D displaces G-actin from MKL and jasplakinolide
 201 stabilizes F-actin²⁴, reducing G-actin) (**Fig. 4B, C**). In all cases, MKL1 nuclear localization
 202 was only modest despite a robust SRF-dependent MYH9 transcriptional response (**Fig.**
 203 **4D, E**). Our data therefore point to a feedback mechanism between actin cytoskeletal
 204 organization and MYH9 transcription and suggest that the threshold of nuclear MKL1
 205 levels necessary for activation of endogenous SRF/MKL targets may be lower than
 206 commonly expected.

207

208 **MYH9 expression is stabilized by a translational buffering system**

209 Given the fact that persistent MYH9 upregulation leads to excessive intracellular forces
 210 that contort cell nuclei and possibly contributes to cancer, we wondered if there were any
 211 post-transcriptional expression mechanisms that might counter the strong transcriptional
 212 induction seen after cofilin/ADF silencing. As a first check, we plotted total myosin-2A
 213 protein levels versus the number of cytoplasmic mRNA in eMyo2AGFP cells. This
 214 revealed a positive correlation in control conditions, but only a weak correlation after
 215 cofilin/ADF silencing (Pearson $r = 0.61$ vs 0.11 , **Fig. 5A**). Regression slopes indicated a
 216 reduced rate of change of MYH9 protein to mRNA (slope = 2.3×10^7 vs 2.9×10^6),
 217 suggesting some form of protein buffering, either at the level of mRNA translation or
 218 protein decay.

219 To see which of these was at play, we quantified the number and intensity of translation
 220 sites in control and cofilin/ADF silenced cells. Knockdown of cofilin/ADF resulted in a 3.5-
 221 fold increase in MYH9 translation sites (**Fig. 5B, C**). Consistent with translational

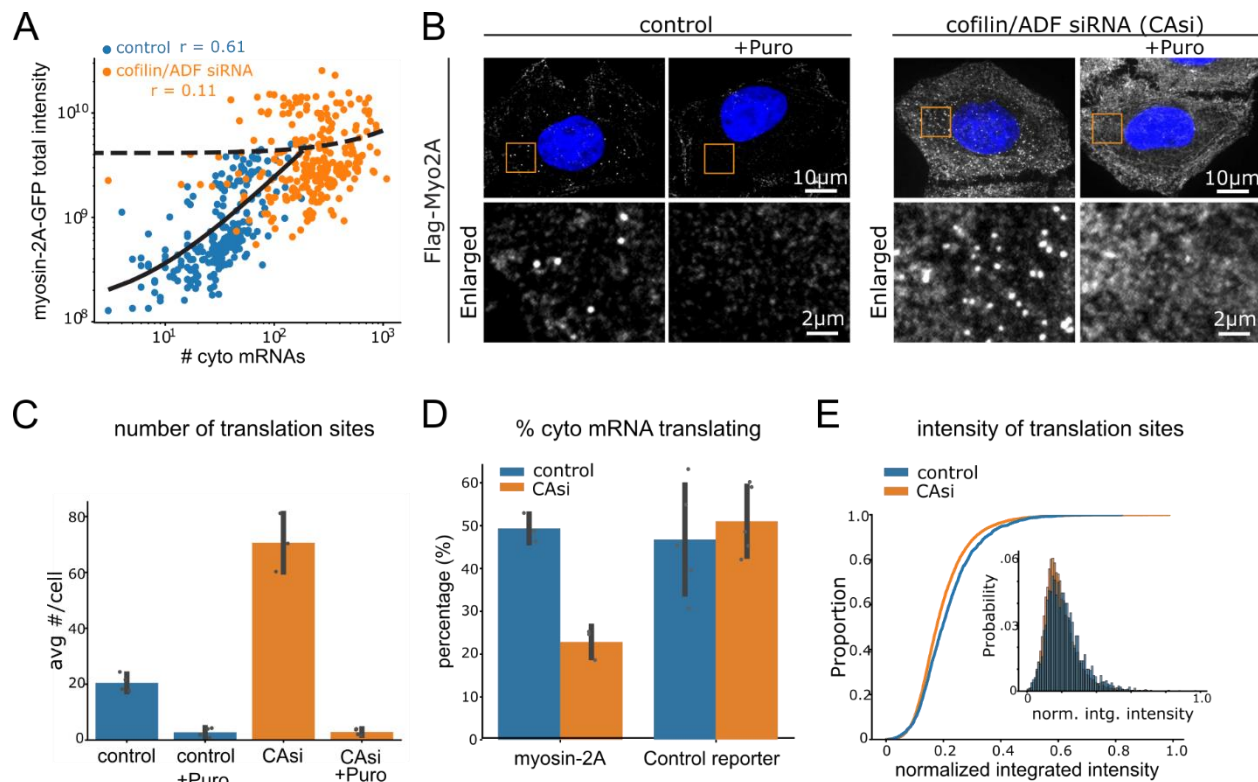


Fig. 5 Depletion of actin depolymerizing proteins results in MYH9 translational buffering . A. Log scale correlation plot of per cell cytoplasmic MYH9 mRNAs vs total myosin-2A-GFP intensity with control or cofilin/ADF siRNA (CA) treatments. **B and C.** Confocal immunofluorescence images (B) and quantification (C) of anti-Flag labeled MYH9 translation sites. Boxed regions are shown in enlargements. Values are mean \pm SD, $n \geq 201$ cells/treatment. **D.** Proportion of translating myosin-2A or KDM5B control mRNAs. Mean \pm SD, $n \geq 209$ cells/treatment. **E.** Cumulative distribution functions and histogram (inset) of normalized translation site intensity, control $n=165$ cells and 2098 translation sites, cofilin/ADF siRNA (CA) $n = 174$ cells and 7272 translation sites.

222 buffering, the fraction of cytoplasmic mRNA that were being translated was reduced by a
223 factor of more than two (**Fig. 5D**). We did not detect a similar decrease in translation
224 efficiency for a control translation reporter, HA-KDM5B-MS2 (**Fig. 5D**), suggesting the
225 reduction in translation efficiency is not global. Interestingly, although we expected the
226 intensity of individual MYH9 translation sites to also be reduced, this was not the case
227 (**Fig. 5E**). Instead, their intensities remained similar, suggesting whatever form MYH9
228 translational buffering takes, it operates more like an on/off switch than a dimmer. In
229 conclusion, our data demonstrate MYH9 is regulated by a translational buffering system
230 that stabilizes MYH9 expression under conditions of persistent transcriptional
231 upregulation, presumably to delay the detrimental effects of myosin-2A overexpression.

232

233 ***MYH9 transcription and translation cooperate upon serum stimulus and are both*** 234 ***required for actomyosin remodeling***

235 Given our previous results we wondered if translational buffering is a universal feature of
236 MYH9 expression. Growth factor stimulation produces rapid (< 30 min) actomyosin
237 cytoskeletal reorganization concurrent with SRF transcriptional activation ²⁵⁻²⁷. How
238 transcription is coupled with translation to this physiologic cue, and whether new protein
239 synthesis may contribute to the near-term cytoskeletal response remain unknown.

240 To address these questions, we serum starved eMyo2AGFP cells and then re-exposed
241 them to serum, measuring total MYH9 mRNA and protein production (**Fig. 6A, B**). This
242 led to rapid actomyosin rearrangements, including the formation of circumferential
243 actomyosin bundles after one hour and an increase in the numbers of ventral stress fibers
244 over the central portion of cells over a period of three hours (**Fig. 6A**). Serum stimulation
245 produced a transient elevation of MYH9 transcription that peaked at 1h post stimulation,
246 as evidenced by an increase in the burst fraction (**Fig. 6C, S4D**). Unlike the translational
247 buffering we observed upon cofilin/ADF silencing, serum stimulation did not significantly
248 alter the fraction of translating cytoplasmic mRNAs (**Fig. 6C**). Instead, the numbers of
249 MYH9 translation sites continued to increase in tandem with the number of cytoplasmic
250 mRNA (**Fig. 6C, S4G**). Furthermore, a modest positive linear correlation between MYH9
251 protein and mRNA levels was maintained at this post-stimulus timepoint (**Fig. S4A**,
252 Pearson $r = 0.37$ vs 0.43).

253 Altogether, these data suggest that MYH9 translation does not always counter the
254 transcriptional response, implying translational buffering is context-dependent.

255 Since serum stimulation activates MYH9 transcription, we evaluated whether SRF-
256 dependent transcription and new protein synthesis contributed to actomyosin cytoskeletal
257 reorganization following this stimulation. Transient MYH9 transcriptional activation, and
258 increased levels of its mRNAs and translation sites were all abrogated by silencing of
259 SRF (**Fig. S4C-F**). Notably, while SRF silencing or inhibition of translation with puromycin
260 did not prevent formation of peripheral actomyosin bundles at 1h post serum stimulation
261 (**Fig. S4C**), both treatments disrupted formation of stress fibers over the central portion

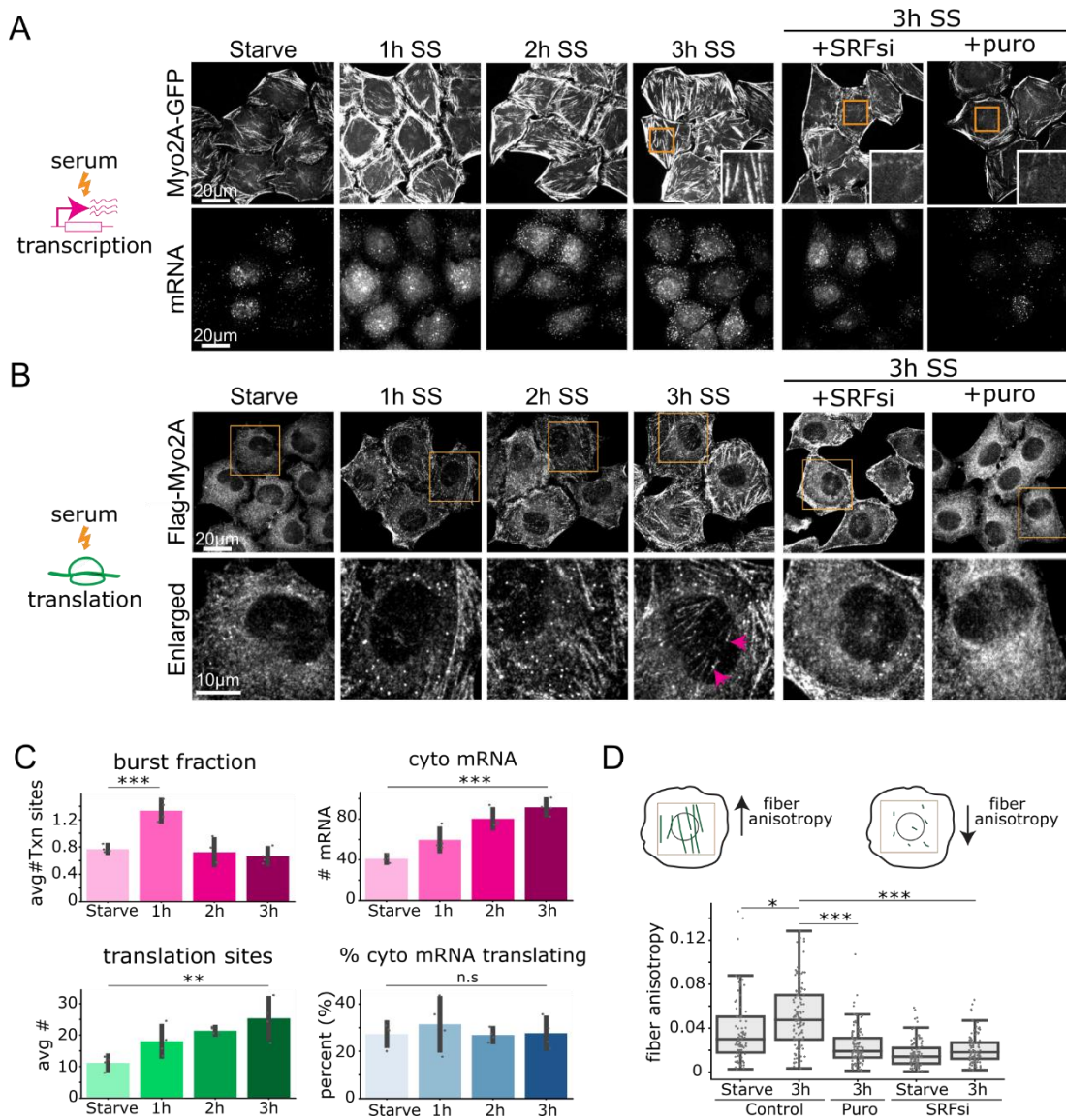


Fig. 6 Transcription and translation work together to establish cellular phenotype upon serum stimulation. A. Confocal fluorescence images depicting actomyosin cytoskeletal rearrangements and MYH9 mRNAs following serum stimulation (SS). Boxed regions, shown enlarged in insets, exemplify loss of central stress fibers at 3h SS following SRF siRNA or puromycin treatments. **B.** Immunofluorescence images of anti-Flag labeled myosin-2A translation. Boxed regions are shown enlarged in lower panels. Note presence of translation spots associated with a central stress fiber (3h SS, magenta arrowheads). **C.** Quantification of transcription and translation features, values are mean \pm SD, n \geq 156 cells/treatment. **D.** Illustration and measurements of central stress fiber ordering. *p < 0.05, **p \leq 0.01, ***p \leq 0.001, n.s, not significant, Welch's t-test. See also Fig. S4.

262 of cells by 3h post serum stimulation (**Fig. 6A, B**), resulting in reduced linear fiber ordering
 263 (**Fig. 6D**). These results suggest that spatial actomyosin stress fiber assembly, within a
 264 window of 3h following growth factor stimulus, requires both SRF-dependent transcription
 265 and new protein synthesis. Furthermore, the presence of MYH9 translation sites along
 266 central stress fibers at 3h post stimulation (**Fig. 6B**, magenta arrowheads) is consistent
 267 with a model of localized MYH9 protein synthesis contributing to assembly of these
 268 structures. Interestingly, while total levels of MYH9 protein increased marginally following
 269 serum stimulation, this remained below statistical significance at the 3h timepoint (**Fig.**

270 **S4B**). This result is also in accord with a conclusion that new MYH9 protein synthesis
271 may not be required to support global actomyosin activity but rather to localized ones.
272 Changes to myosin-2A protein turnover during this period could contribute to such an
273 outcome.

274

275 **Discussion**

276 Homeostatic maintenance of protein levels is an overarching feature of gene expression,
277 but the hidden regulatory mechanisms that maintain homeostasis have been difficult to
278 study and verify. By engineering a novel cell line in which all aspects of MYH9 activity can
279 be visualized in separate colors and with single-molecule precision, we discovered a
280 highly dynamic and multilayered regulatory network lying beneath the apparent stability
281 of myosin-2A expression.

282 Much like a thermostat maintains temperature, our study provides evidence that MYH9
283 translation is a key regulatory checkpoint that ensures myosin-2A levels are acceptable.
284 In steady state, nearly every cytoplasmic MYH9 mRNA is translated to meet the demands
285 of the actomyosin cytoskeleton. However, in scenarios when myosin-2A levels become
286 too high, such as when transcription is persistently elevated upon loss of actin
287 depolymerizing proteins like cofilin, translation efficiency is down regulated. Such
288 translational buffering stabilizes protein production to minimize the damaging effects of
289 excessive myosin. Similarly, during cell division, MYH9 translational buffering counters a
290 sharp transcriptional burst. Specific lowering of MYH9 translation during mitosis may
291 safeguard against defects such as impaired karyokinesis, as observed in cofilin-depleted
292 cells with excessive myosin activation ¹⁵. Conversely, in scenarios that elevate
293 actomyosin assembly, such as the recovery from serum starvation, MYH9 translation
294 aligns with transcription. This is necessary to rapidly remodel the actomyosin cytoskeleton
295 so cellular equilibrium can be quickly reestablished. Thus, depending on the precise
296 cellular context, our data argue MYH9 translational regulation can either facilitate or buffer
297 the transcriptional response to help ensure myosin-2A levels stay within an acceptable
298 range.

299 While we were unable to pinpoint the precise molecular mechanism behind MYH9
300 translational buffering, our study offers some clues. First, the default mode of MYH9
301 translation seems to be the ON state, since the vast majority of transcripts appear to be
302 translated throughout interphase. Second, the observation that buffering can more than
303 halve the fraction of translating cytoplasmic MYH9 mRNA while leaving their intensities
304 relatively unchanged suggests buffering acts more like a binary on/off switch than a
305 gradual fader. These observations hint at the possible involvement of specific RNA-binding
306 proteins or post-transcriptional modifications that selectively silence MYH9 mRNA.
307 Identifying these specific factors will be an interesting avenue of future research, although
308 a major challenge will be sorting myosin-specific regulators from other targets of the broad
309 SRF/MKL nexus ²⁸.

310 A striking finding of our study is that a just-in-time mode of local protein synthesis appears
311 necessary for assembly of certain actomyosin stress fibers within a 3h period following
312 growth factor stimulation. This result was surprising for at least two reasons. First, growth
313 factor signaling produces rapid stress fiber assembly within 20 minutes of stimulus,
314 suggesting transcription and global new protein synthesis are not required for immediate
315 actomyosin remodeling^{25, 26}. Consistent with this view, peripheral actomyosin bundling
316 within 1h of serum stimulus was not lost by perturbations to MYH9 transcription or through
317 protein synthesis inhibition. Secondly, a requirement for new protein synthesis occurred
318 during a period where total MYH9 protein levels did not change significantly. As such, bulk
319 level assays of protein amounts would not have foreshadowed a need for new MYH9
320 protein synthesis. Nevertheless, loss of central stress fibers at 3h post stimulus, through
321 either inhibition of SRF transcription or protein synthesis, suggested a requirement for
322 both new mRNA transcripts and local translation, similar to what has been observed for
323 actin ²⁹. De novo mRNA and protein synthesis of MYH9 and other SRF targets may
324 therefore be a means to specify a distinct population of molecules, without previous
325 modifications, for current localized use.

326 At the level of transcription, our study sheds light on the elusive molecular pathways that
327 link cofilin inactivation and myosin overactivity. Central to this pathway is MKL, a
328 transcription factor that activates MYH9 via SRF but whose translocation into the nucleus
329 is inhibited by G-actin. According to our data, depletion of the actin depolymerizing
330 proteins cofilin and ADF lowers G-actin levels, leading to MKL nuclear translocation and
331 enhanced transcriptional activation of MYH9. Left unchecked, this leads to excessive
332 myosin contractile forces that, despite the presence of translational buffering, eventually
333 lead to severe morphological aberrations in cells and potentially oncogenic
334 transformations ³⁰. Our combined data therefore provide a compelling molecular pathway
335 that would link cofilin-inactivation, higher myosin expression and activity, translational
336 buffering, and disease states.

337 Having demonstrated the potential of eMyo2AGFP cells, we envision many possible
338 applications. They hold especially great promise for screening purposes, where they can
339 help uncover hidden gene regulatory dynamics. While powerful, there are several caveats
340 to their use worth highlighting. First, it can be technically challenging to detect dimmer
341 myosin-2A translation sites due to the abundance of background signal from mature
342 myosin-2A. While we used the lack of a GFP signal to distinguish translation sites from
343 mature structures, the high background could still be problematic. We therefore
344 recommend measurements of translation efficiency be made in fixed rather than live cells,
345 where FLAG binding sites can be fully saturated and background signal minimized.
346 Second, although we were able to insert mRNA and GFP tags into both MYH9 alleles, we
347 only succeeded in inserting FLAG tags into one allele. This leaves a hidden translation
348 fraction in eMyo2AGFP cells that can only be indirectly assessed. While we believe the
349 hidden fraction behaves similarly to the tagged fraction since we detected translation from
350 nearly half the mRNA, we cannot rule out the possibility that the hidden fraction behaves
351 differently. Third, it remains unclear to what extent our approach can be generalized to

352 other cell lines or other genes. Some cells may be difficult to CRISPR edit and some
353 genes may not tolerate tagging. Keeping these caveats in mind, we believe eMyo2AGFP
354 cells represent a significant advance and should be of broad interest to those wishing to
355 explore the intricacies of gene regulation in the context of cellular perturbations of any
356 kind.

357

358 **Methods**

359 *Cell Culture and Drug Treatments*

360 Human HeLa-kyoto cells were obtained from ATCC and maintained in high glucose
361 DMEM supplemented with 10% fetal bovine serum (Atlas). For translation inhibition cells
362 were treated at 50 μ g/ml with puromycin (Sigma) for 20 min or as otherwise indicated.
363 Cells for MKL nuclear-cytoplasmic assessment were treated with 2 μ M cytochalasin D
364 (Cayman Chemical), 1 μ M Jasplakinolide (Cayman Chemical) or dimethyl sulfoxide
365 (Sigma) for controls, for 2h prior to fixation for analyses. For serum stimulation
366 experiments cells were starved for 18-24 h in medium containing 0.3% serum and
367 stimulated by replacing with medium containing 15% serum.

368 *Gene Editing*

369 Sequential rounds of CRISPR/Cas9 gene editing of the endogenous MYH9 gene locus
370 located on chromosome 22 was performed as previously detailed ³¹. Briefly, guide RNAs
371 targeting the start ATG or stop codons of coding exons 1 and 40, respectively, were cloned
372 into plasmid pX330-U6-Chimeric_BB-CBh-hSpCas9. For C-terminal tagging a homology
373 directed repair donor plasmid containing mClover3 (derived from Addgene plasmid
374 72829), followed by 24xMS2V5 ³² was created. For N-terminal tagging a repair donor
375 plasmid consisting of mCherry2 (derived from Addgene plasmid # 72831), flanked by a
376 total of 6X Flag repeat epitope tags was generated. Plasmids for Cas9 and homology
377 repair were transfected to cells with Lipofectamine 2000 (Invitrogen). Successful C-
378 terminal knock-in cells were identified by fluorescence activated cell sorting (FACS) and
379 confirmed by both visual inspection and genomic DNA PCR genotyping, as described ³³.
380 A clone with two C-terminal knock-in alleles was transfected with Cas9 and N-terminal
381 homology repair plasmids, followed by FACS to isolate dual mCherry2 and mClover
382 positive edited cells. PCR genotyping revealed that all N-terminal knock-in clones had
383 only one of two alleles successfully incorporating 6xFlag-mCherry2. PCR primers to
384 detect the wild type locus could also discriminate a larger product corresponding to the
385 recombinant allele, however, wild type test reactions were optimized and used only to
386 detect the presence of wild type alleles.

387 *siRNA*

388 Control siRNA oligonucleotides to luciferase and siRNAs cofilin and ADF were as
389 previously described and characterized. siRNAs to SRF were from Ambion (#13429) and
390 GCGTGAAGA TCA AGATGGA obtained from Qiagen. Cells were transfected 50 nM of
391 siRNAs with Lipofectamine RNAiMax according to manufacturer's instructions.

392 *smiFISH*

393 Cells were fixed for 20 min at room temp in 4% paraformaldehyde (Electron Microscopy
394 Sciences) in PBS, washed in PBS and permeabilized in 70% ethanol overnight at 4 °C. A
395 set of 30 probes spanning the entire coding sequence of human MYH9 were designed
396 using Oligostan software ³⁴ and obtained from IDT. Probes were prepared and annealed

397 according to ref 34, mixed with hybridization buffer (Stellaris) and incubated with cells
398 overnight at 37°C. Cells were washed 3x over 30 min in Wash Buffer A (Stellaris), washed
399 once with Wash Buffer B (Stellaris) and mounted for imaging.

400 *Fluorescence staining*

401 We selected a clone of C-terminally Clover-24xMS2 tagged MYH9 cells that stably
402 expressed Halo-MCP at relatively low levels for visualization of endogenous MYH9
403 mRNAs. Prior to imaging of mRNAs cells were exposed to 200 nM JF646 HaloTag ligand
404 (Promega) for 20 mins. Cells grown on glass coverslips were fixed in 4% formaldehyde
405 in CBS buffer (10 mM 4-Morpholineethanesulfonic acid, pH 6.1, 138 mM KCl, 3 mM
406 MgCl₂, 2 mM ethyleneglycol-bis(β-aminoethyl)-N,N,N',N'-tetraacetic acid, 0.32 M
407 sucrose) for 20 min at room temperature. mRNAs and cytoskeletal structures were best
408 visualized by inclusion of 0.3% Triton X-100 in the fix buffer. This cytoskeletal fixation
409 procedure enhanced myosin-2A labeling in cytoskeletal structures but resulted in less
410 focal labeling of translation sites as detected by anti-Flag. For best quantitative measures
411 of mRNAs and translation sites replicate coverslips were fixed with and without inclusion
412 of Triton X-100 to visualize mRNAs and translation sites independently. Translation sites
413 in fixed cells were labeled anti-Flag labeling (FUJIFILM, Wako) followed by Cy3 or Alexa
414 594 conjugated anti-mouse secondary antibodies (Jackson Immunoresearch and
415 Invitrogen). In live cells, translation sites were labeled by bead loading Flag-Cy3 Fab
416 antibody fragments as previously described³⁵. Cy3-Flag antibodies detect nascent Flag-
417 MYH9 proteins where both mCherry and mClover signals are absent due to the delay in
418 fluorescence protein maturation. Other antibodies were MKL1 (NBP2-45862, Novus
419 Biologicals; sc-32909 Santa Cruz Biotechnology), SRF (66742-1, Proteintech), GAPDH
420 (MAB 374, Millipore), Sun2 (HPA001209, Sigma). DNA was labeled by 4',6-diamidino-2-
421 phenylindole (DAPI). Mitotic cells were classified based on visual inspection of DAPI
422 labeling.

423 Cells co-transfected with either control or cofilin/ADF siRNAs and an HA-KDM5B-MS2
424 translation reporter⁴ were fixed by the cytoskeletal fixation procedure described above.
425 Cells were labeled for translation by anti-HA antibodies (12CA5, Roche) and with JF646
426 HaloTag ligand for mRNAs.

427 *Microscopy*

428 Confocal images were captured on an Olympus IX8 spinning disk microscope with a
429 CSU22 head, equipped with 405, 488, 561 and 640 nm laser lines. Objectives were either
430 100x/1.40 NA or 60x/1.42 NA. Images were acquired with an iXon Ultra 888 EMCCD
431 camera (Andor) using SlideBook (Intelligent Imaging Innovations). Images of fixed cells
432 were acquired as z-stacks at 0.3 μm intervals.

433 Cells were plated on glass bottom 35 mm dishes in an enclosed chamber at 37°C and
434 with 5% CO₂ for confocal live cell imaging. 11-15 z-planes were acquired at 0.5 μm steps
435 at time intervals between 5 and 10 minutes for evaluations of MYH9 transcription. Live
436 cell translation images were captured as volumes 7-10 z-planes, at 0.65 μm steps and

437 time intervals of 2-10 seconds. Some live cell images were captured on a custom built
438 highly inclined and laminated optical sheet (HILO) microscope ⁴ at similar or faster capture
439 rates.

440 *Morphometric measurements*

441 Cell, nuclear and cytoplasmic measurements were obtained from 2D segmentations
442 produced using Cellpose software ³⁶. Cell masks were obtained using the 'cyto' model
443 where image channels marking both cells and DAPI labeled nuclei were utilized. Nuclear
444 masks were generated using the 'nuclei' model. Integrated intensity measurements were
445 computed using measures over entire z-stacks from background subtracted images,

446 Measurements of myosin stress fiber ordering through filament anisotropy was done
447 using FibrilTool ³⁷. A rectangular ROI covering the central portion, over the entire nucleus,
448 of individual cells was applied to images of ventral actomyosin filaments for
449 measurements.

450 *Translation site and mRNA Quantification*

451 A subset of maximum intensity z-projections of control or puromycin treated cells, stained
452 with anti-Flag, were used to annotate translation sites for interactive pixel classification
453 machine learning using Ilastik software ³⁸. Visually, translation sites were apparent as
454 bright rounded focal spots. All available features from Color/Intensity, Edge and Texture
455 at scales up to smoothing sigma = 5 were selected. Annotations were made for three
456 classes including, background, translation sites and cell. The trained model was used to
457 generate translation site prediction maps for each experimental dataset, that were then
458 segmented in ImageJ to generate centroid coordinates for each detected site. Intensity
459 measurements were made from a central circular ROI with a radius of 4 pixels, using
460 measurements from a 1-2 pixels ROI extension for localized background subtraction.
461 Where indicated, intensity values were normalized between 0 and 1 for all treatments
462 within a replicate.

463 Images of labeled mRNAs were processed in 3D using FISH-quant v2 ³⁹ for detection
464 and quantification of single mRNAs and nuclear mRNA clusters corresponding to
465 transcription sites. A standard FISH-quant pipeline consisted of application of a Laplacian
466 of Gaussian filter to raw mRNA images, followed by spot detection with parameters: voxel
467 size (nm) in 3D = (300, 95, 95), object radius (nm) = (350, 150, 150) and a threshold
468 scaling value of 1.2. Cluster detection values: radius = 350 nm and minimum # spots = 3.
469 Translation sites and mRNAs were mapped to individual cells and nuclei using
470 segmentations of both structures generated by Cellpose. Code from scripts used for
471 image analysis is available at <https://github.com/Colorado-State-University-Stasevich-Lab>.

473

474 *Live cell transcription and translation time series analysis*

475 Transcription sites could be identified as bright pulsatile nuclear spots with intensities
476 greater than three times the mean of single nuclear mRNAs. Visually, cells with
477 transcriptional activity could be readily identified from time series projections of nuclear
478 mRNA distribution. Transcription sites were tracked over time using semi-automated
479 tracking with ImageJ TrackMate ⁴⁰. Frames in which the tracked spot was absent were
480 assigned the position of the last previous observed spot position. Trajectories of spot
481 intensities measured over a 7-pixel radius from spot centroids were used for classification
482 of ON/OFF periods using a Hidden Markov Model (HMM) as introduced previously ¹⁸. We
483 applied a three-state model in line with an earlier report ⁴¹. The GaussianHMM function
484 from the python library hmmlearn was used to compute the HMM states for individual
485 transcription site intensity traces.

486 Tracks of translation site motility were generated with TrackMate and mean squared
487 displacement (MSD) measurements computed using opensource TrackPy.

488

489 *Statistical Analysis*

490 Data were tabulated from the results of three to eight experiments, with overlap between
491 datasets for some individual plots such as figures 1E and 5C. P-values were computed
492 using the Welch's t-test.

493

494 **Acknowledgements**

495 We wish to thank Nick Pollock, Ning Zhao and James Bamburg for help with reagents,
496 Luis Aguilera for assistance with computational analyses, Tatsuya Morisaki for scientific
497 discussions and assistance with microscopy and members of the group for their input.
498 This work was supported by grants from the National Institutes of Health (R35GM119728
499 and R56AI155897) and the National Science Foundation (MCB-1845761).

500

501 **Competing interests**

502 The authors declare no competing interests.

503 **References**

504

- 505 1. Yan, X., Hoek, T.A., Vale, R.D. & Tanenbaum, M.E. Dynamics of Translation of Single
506 mRNA Molecules In Vivo. *Cell* **165**, 976-989 (2016).
- 507 2. Wu, B., Eliscovich, C., Yoon, Y.J. & Singer, R.H. Translation dynamics of single mRNAs in
508 live cells and neurons. *Science* **352**, 1430-1435 (2016).
- 509 3. Wang, C., Han, B., Zhou, R. & Zhuang, X. Real-Time Imaging of Translation on Single
510 mRNA Transcripts in Live Cells. *Cell* **165**, 990-1001 (2016).
- 511 4. Morisaki, T. *et al.* Real-time quantification of single RNA translation dynamics in living cells.
512 *Science* **352**, 1425-1429 (2016).
- 513 5. Morisaki, T., Wiggan, O. & Stasevich, T.J. Translation Dynamics of Single mRNAs in Live
514 Cells. *Annual review of biophysics* (2023).
- 515 6. Buccitelli, C. & Selbach, M. mRNAs, proteins and the emerging principles of gene
516 expression control. *Nature reviews. Genetics* **21**, 630-644 (2020).
- 517 7. Pecci, A., Ma, X., Savoia, A. & Adelstein, R.S. MYH9: Structure, functions and role of non-
518 muscle myosin IIA in human disease. *Gene* **664**, 152-167 (2018).
- 519 8. Eisenberg, E. & Levanon, E.Y. Human housekeeping genes, revisited. *Trends Genet* **29**,
520 569-574 (2013).
- 521 9. Amano, M. *et al.* Phosphorylation and activation of myosin by Rho-associated kinase
522 (Rho-kinase). *J.Biol.Chem.* **271**, 20246-20249 (1996).
- 523 10. Nguyen, L.T.S., Jacob, M.A.C., Parajón, E. & Robinson, D.N. Cancer as a biophysical
524 disease: Targeting the mechanical-adaptability program. *Biophysical journal* **121**, 3573-
525 3585 (2022).
- 526 11. Wang, Y., Liu, S., Zhang, Y. & Yang, J. Myosin Heavy Chain 9: Oncogene or Tumor
527 Suppressor Gene? *Medical science monitor : international medical journal of experimental
528 and clinical research* **25**, 888-892 (2019).
- 529 12. Medjkane, S., Perez-Sanchez, C., Gaggioli, C., Sahai, E. & Treisman, R. Myocardin-
530 related transcription factors and SRF are required for cytoskeletal dynamics and
531 experimental metastasis. *Nat Cell Biol* **11**, 257-268 (2009).
- 532 13. Pichon, X. *et al.* Visualization of single endogenous polysomes reveals the dynamics of
533 translation in live human cells. *J Cell Biol* **214**, 769-781 (2016).
- 534 14. Stonyte, V., Boye, E. & Grallert, B. Regulation of global translation during the cell cycle. *J
535 Cell Sci* **131** (2018).
- 536 15. Wiggan, O., Shaw, A.E., DeLuca, J.G. & Bamburg, J.R. ADF/cofilin regulates actomyosin
537 assembly through competitive inhibition of myosin II binding to F-actin. *Developmental
538 Cell* **22**, 530-543 (2012).
- 539 16. Wiggan, O., Schroder, B., Krapf, D., Bamburg, J.R. & DeLuca, J.G. Cofilin Regulates
540 Nuclear Architecture through a Myosin-II Dependent Mechanotransduction Module.
541 *Scientific reports* **7**, 40953 (2017).
- 542 17. Verdoni, A.M., Aoyama, N., Ikeda, A. & Ikeda, S. Effect of destrin mutations on the gene
543 expression profile in vivo. *Physiological genomics* **34**, 9-21 (2008).
- 544 18. Larson, D.R. *et al.* Direct observation of frequency modulated transcription in single cells
545 using light activation. *eLife* **2**, e00750 (2013).
- 546 19. Tunnacliffe, E. & Chubb, J.R. What Is a Transcriptional Burst? *Trends Genet* **36**, 288-297
547 (2020).
- 548 20. Dar, R.D. *et al.* Transcriptional burst frequency and burst size are equally modulated
549 across the human genome. *Proc Natl Acad Sci U S A* **109**, 17454-17459 (2012).
- 550 21. Kalo, A. *et al.* Cellular Levels of Signaling Factors Are Sensed by β -actin Alleles to
551 Modulate Transcriptional Pulse Intensity. *Cell reports* **11**, 419-432 (2015).

552 22. Olson, E.N. & Nordheim, A. Linking actin dynamics and gene transcription to drive cellular
553 motile functions. *Nature reviews. Molecular cell biology* **11**, 353-365 (2010).
554 23. Schofield, A. & Bernard, O. LIM Kinase and Cancer Metastasis, in *Cytoskeleton and*
555 *Human Disease*. (ed. M. Kavallaris) 159-168 (Humana Press, Totowa, NJ; 2012).
556 24. Miralles, F., Posern, G., Zaromytidou, A.I. & Treisman, R. Actin dynamics control SRF
557 activity by regulation of its coactivator MAL. *Cell* **113**, 329-342 (2003).
558 25. Ridley, A.J. & Hall, A. The small GTP-binding protein rho regulates the assembly of focal
559 adhesions and actin stress fibers in response to growth factors. *Cell* **70**, 389-399 (1992).
560 26. Hill, C.S., Wynne, J. & Treisman, R. The Rho family GTPases RhoA, Rac1, and CDC42Hs
561 regulate transcriptional activation by SRF. *Cell* **81**, 1159-1170 (1995).
562 27. Chrzanowska-Wodnicka, M. & Burridge, K. Rho-stimulated contractility drives the
563 formation of stress fibers and focal adhesions. *J.Cell Biol.* **133**, 1403-1415 (1996).
564 28. Esnault, C. *et al.* Rho-actin signaling to the MRTF coactivators dominates the immediate
565 transcriptional response to serum in fibroblasts. *Genes Dev* **28**, 943-958 (2014).
566 29. Yoon, Y.J. *et al.* Glutamate-induced RNA localization and translation in neurons. *Proc Natl*
567 *Acad Sci U S A* **113**, E6877-e6886 (2016).
568 30. Takaki, T. *et al.* Actomyosin drives cancer cell nuclear dysmorphia and threatens genome
569 stability. *Nature communications* **8**, 16013 (2017).
570 31. Wiggan, O., DeLuca, J.G., Stasevich, T.J. & Bamburg, J.R. Lamin A/C deficiency enables
571 increased myosin-II bipolar filament ensembles that promote divergent actomyosin
572 network anomalies through self-organization. *Mol Biol Cell* **31**, 2363-2378 (2020).
573 32. Wu, B. *et al.* Synonymous modification results in high-fidelity gene expression of repetitive
574 protein and nucleotide sequences. *Genes Dev* **29**, 876-886 (2015).
575 33. Bauer, D.E., Canver, M.C. & Orkin, S.H. Generation of genomic deletions in mammalian
576 cell lines via CRISPR/Cas9. *Journal of visualized experiments : JoVE*, e52118 (2015).
577 34. Tsanov, N. *et al.* smiFISH and FISH-quant - a flexible single RNA detection approach with
578 super-resolution capability. *Nucleic Acids Res* **44**, e165 (2016).
579 35. Cialek, C.A., Galindo, G., Koch, A.L., Saxton, M.N. & Stasevich, T.J. Bead Loading
580 Proteins and Nucleic Acids into Adherent Human Cells. *Journal of visualized experiments*
581 : JoVE (2021).
582 36. Stringer, C., Wang, T., Michaelos, M. & Pachitariu, M. Cellpose: a generalist algorithm for
583 cellular segmentation. *Nature methods* **18**, 100-106 (2021).
584 37. Boudaoud, A. *et al.* FibrilTool, an ImageJ plug-in to quantify fibrillar structures in raw
585 microscopy images. *Nature protocols* **9**, 457-463 (2014).
586 38. Berg, S. *et al.* ilastik: interactive machine learning for (bio)image analysis. *Nature methods*
587 **16**, 1226-1232 (2019).
588 39. Imbert, A. *et al.* FISH-quant v2: a scalable and modular tool for smFISH image analysis.
589 *RNA (New York, N.Y.)* **28**, 786-795 (2022).
590 40. Tinevez, J.Y. *et al.* TrackMate: An open and extensible platform for single-particle tracking.
591 *Methods (San Diego, Calif.)* **115**, 80-90 (2017).
592 41. Senecal, A. *et al.* Transcription factors modulate c-Fos transcriptional bursts. *Cell reports*
593 **8**, 75-83 (2014).

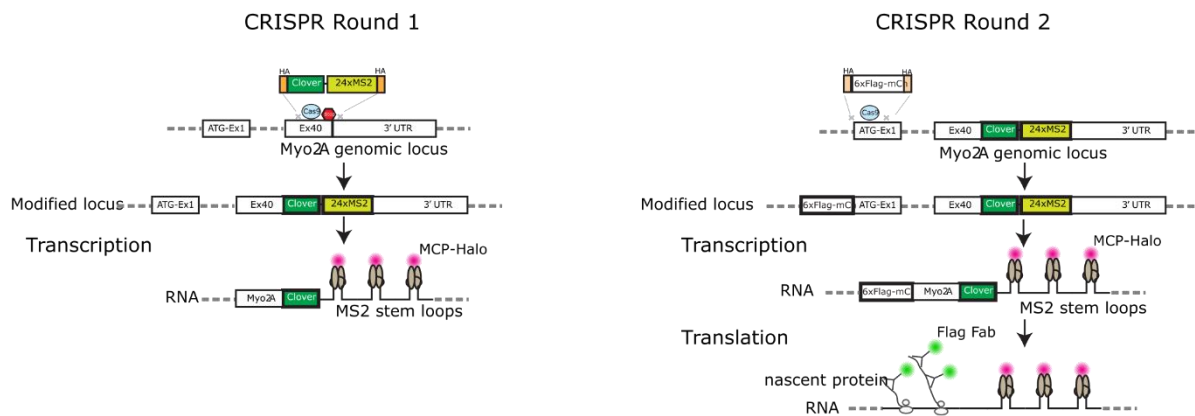
594

595

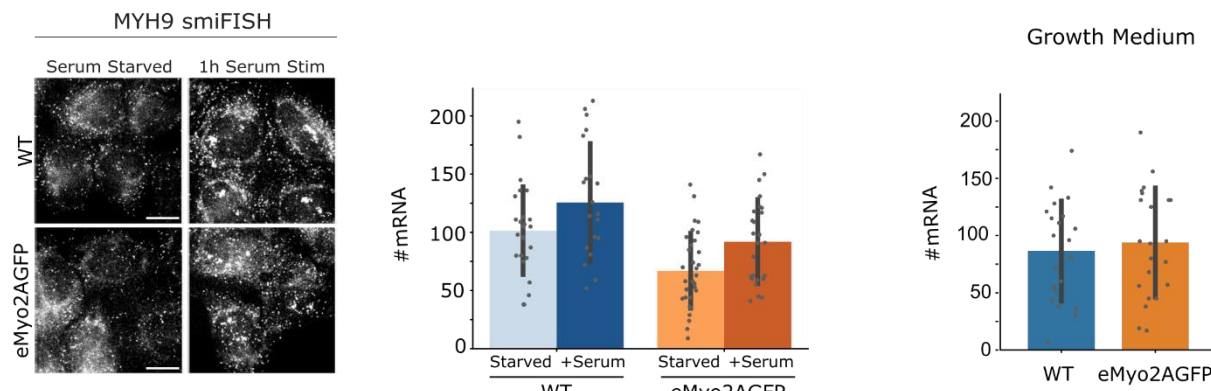
596 **Supplementary Material**

597

A



B



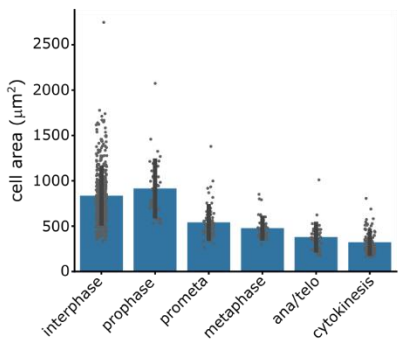
598

599 **Figure S1. CRISPR strategy to tag endogenous MYH9 and smiFISH analysis of**
600 **tagged cells. A. Illustration of sequential gene editing strategy used to generate eMyo2A**
601 **GFP cells. B. Fluorescence images and quantification of MYH9 mRNA labeled by**
602 **smiFISH probes that target both tagged and untagged transcripts. mRNAs were assessed**
603 **under normal growth conditions and following serum stimulation of serum starved cells.**
604 **Values are mean ± SD. Scale bars 10 μm.**

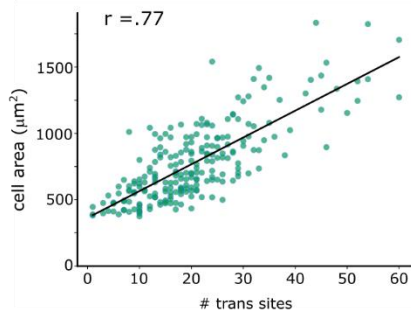
605

606

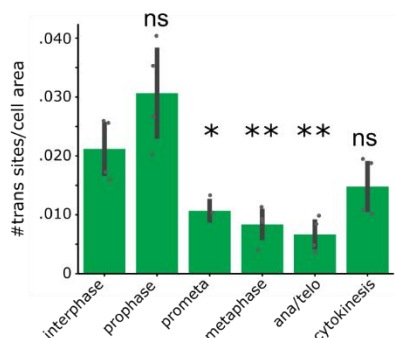
A



B



C



607

608

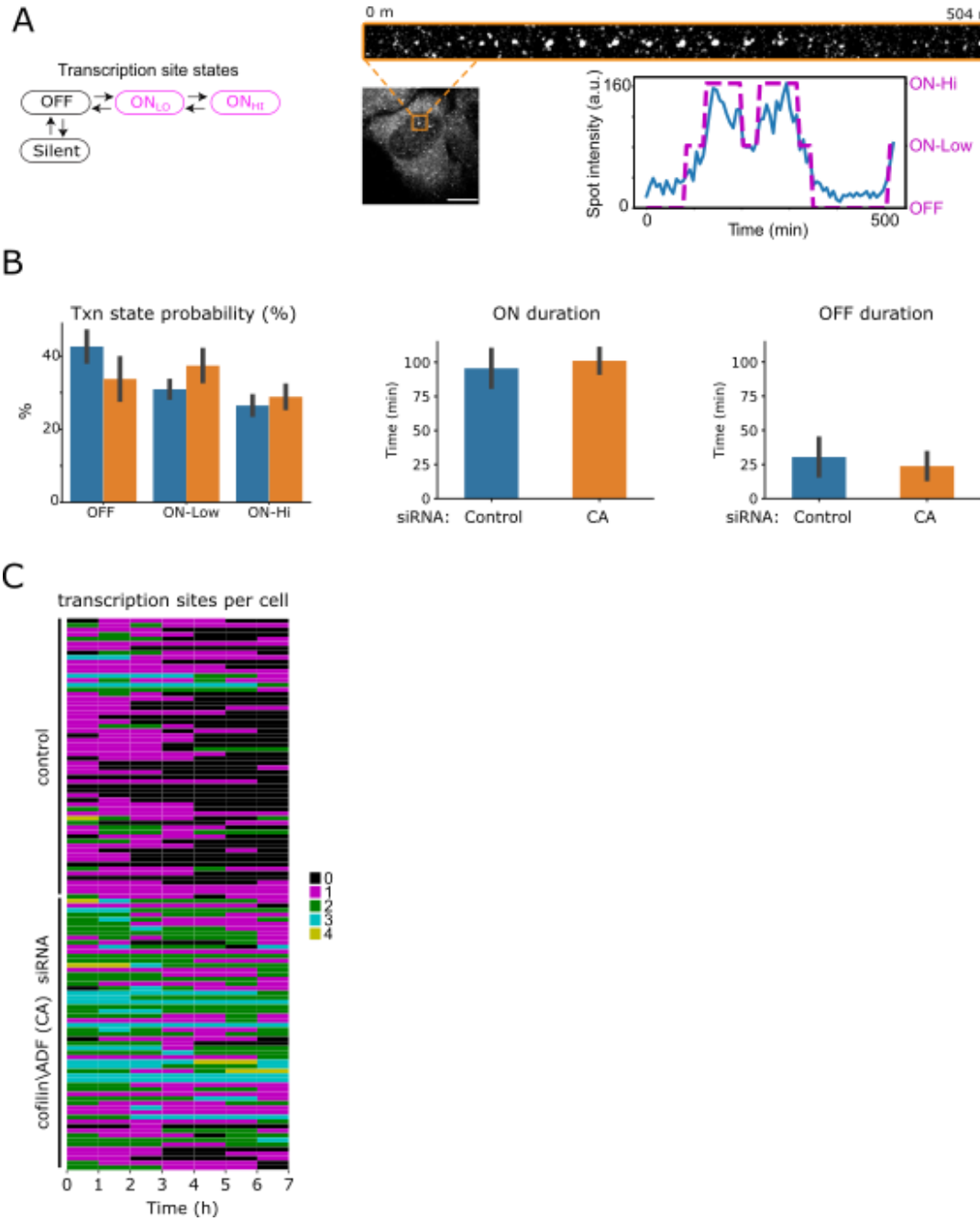
609 **Figure S2. Relationships between MYH9 translation and cell area. A.** Quantification
610 of eMyo2AGFP surface cell area across the cell cycle, mean \pm SD. **B.** Correlation plot of
611 cell area to numbers of MYH9 translation sites, r is Pearson's correlation coefficient. **C.**
612 Quantification of MYH9 translation sites normalized to cell area across the cell cycle,
613 mean \pm SD. * $p < 0.05$, ** $p \leq 0.01$, n.s, not significant, Welch's t-test.

614

615

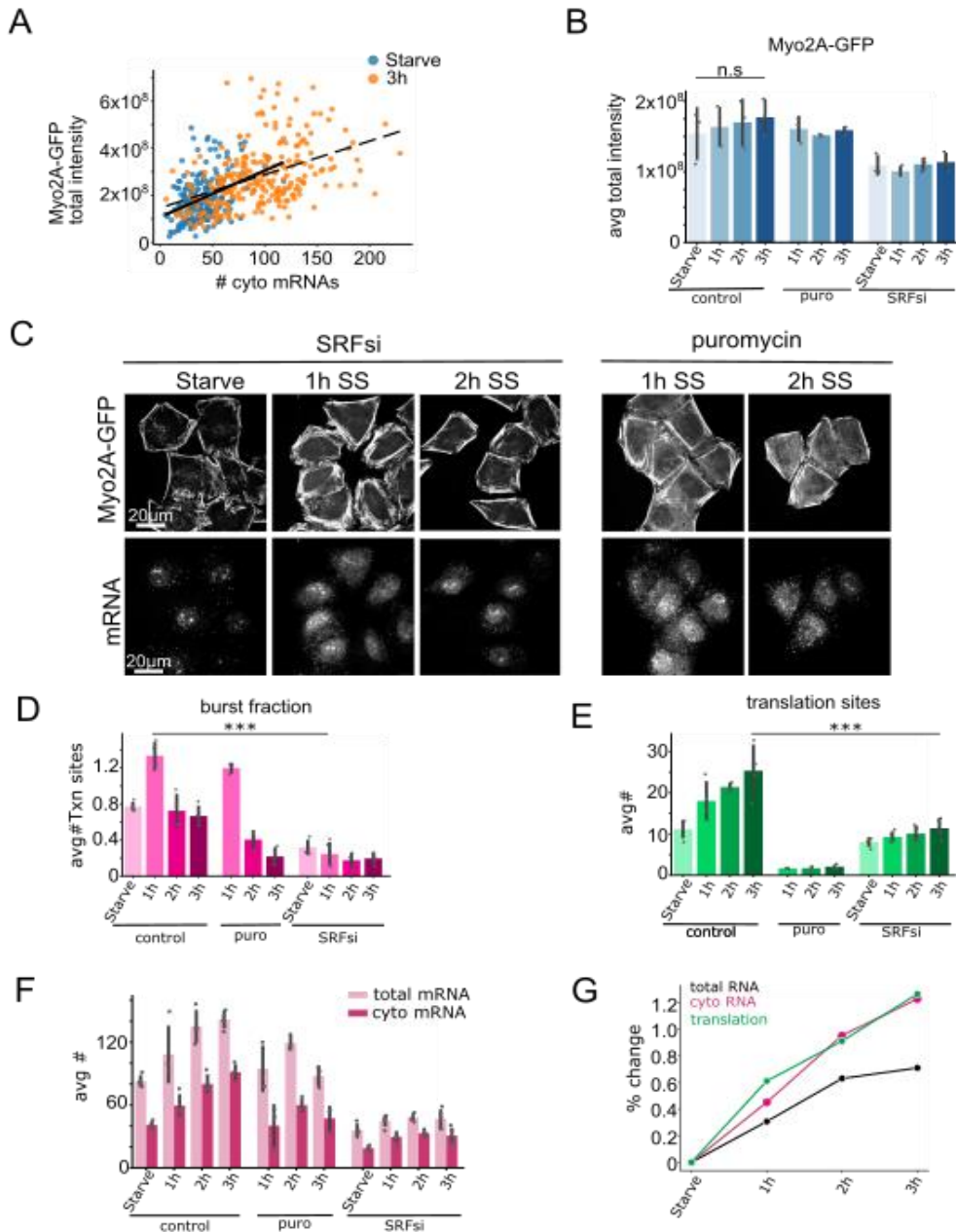
616

617



618

619 **Figure S3. Measurements of MYH9 transcriptional activity in live cells. A.**
620 Hypothetical transcription activity model and example confocal fluorescence images of
621 Halo-MCP labeled MYH9 transcription foci (boxed region) in a time-lapse series. Scale
622 bar 10 μ m. Transcription site intensity trace illustrates classification of on and off states
623 as fit to a hidden Markov model. **B.** Quantification of MYH9 transcription activity dynamics
624 for control or cofillin/ADF siRNA treated eMyo2AGFP cells. Values are mean \pm SD. **C.**
625 Heat map of the number of per cell MYH9 transcription sites over time, with each row
626 corresponding to an individual cell.



627 **Figure S4. Transcription and translation requirements in MYH9 expression for**
628 **cytoskeletal response to serum activation. A.** Correlation plot of integrated Myosin2A-
629 **GFP intensity to cytoplasmic MYH9 mRNAs for eMyo2AGFP cells. Solid line shows linear**
630 **fit to starved condition and dashed line to 3h post serum stimulation. B.** Quantification of
631 **total Myosin2A-GFP intensity. C.** Confocal fluorescence images depicting actomyosin
632 **cytoskeletal rearrangements and MYH9 mRNAs following serum stimulation (SS). D.**
633 **Quantification of the number of per cell MYH9 transcription sites. E.** Quantification of per
634 **cell translation sites. F.** Quantification of MYH9 mRNAs. **G.** Percentage change plot
635 **summarizing data for control treatment from panels E and F. Bar graphs are mean \pm SD.**
636 *****p \leq 0.001, n.s., not significant, Welch's t-test.**

637 Supplementary Movies

638 **Movie S1.** Live cell imaging of an eMyo2AGFP cell with myo2A-GFP protein (green) and
639 mRNA (JF646-Halo-MCP, magenta), boxed region illustrates mRNA transcription focus.
640 Images acquired at 1 frame/second. Related to Fig. 1.

641 **Movie S2.** Live cell imaging of translation from a single mRNA (cyan boxed region,
642 enlarged in spot1) and a mRNA cluster (orange boxed region, enlarged in spot2) in HeLa
643 eMyo2AGFP cells. Translation (trans) and myosin2A protein are labeled by bead loaded
644 Cy3-Flag Fab (green) and mRNAs by JF646-Halo-MCP (magenta). Images are confocal
645 z-stack projections acquired at 0.16 frame (z-volume)/second. Related to Fig. 1.

646 **Movie S3.** Live cell imaging of a MYH9 transcription activity in an eMyo2AGFP cell with
647 mRNA labeled by JF646-Halo-MCP. Images are confocal z-stack projections acquired at
648 7 min intervals. Related to Fig. S3